J. Fluid Mech. (2014), *vol.* 745, *pp.* 300–320.
doi:10.1017/jfm.2014.99

Spanwise reflection symmetry breaking and turbulence control: plane Couette flow

G. Chagelishvili[1,2,4], G. Khujadze[1,3,†], H. Foysi[3] and M. Oberlack[4,5]

[1]Abastumani Astrophysical Observatory, Ilia State University, Tbilisi 0160, Georgia

[2]M. Nodia Institute of Geophysics, Tbilisi State University, Tbilisi 0128, Georgia

[3]Chair of Fluid Mechanics, Universität Siegen, Paul-Bonatz-Str. 9-11, 57068 Siegen, Germany

[4]Chair of Fluid Dynamics, Technische Universität Darmstadt, Darmstadt 64287, Germany

[5]GS Comp. Engineering, Technische Universität Darmstadt, Darmstadt 64287, Germany

(Received 10 May 2013; revised 11 December 2013; accepted 18 February 2014;
first published online 19 March 2014)

We propose and analyse a new strategy of shear flow turbulence control that can be realized by the following steps: (i) imposing specially designed seed velocity perturbations, which are non-symmetric in the spanwise direction, at the walls of a flow; (ii) the configuration of the latter ensures a gain of shear flow energy and the breaking of turbulence spanwise reflection symmetry: this leads to the generation of spanwise mean flow; (iii) that changes the self-sustained dynamics of turbulence and results in a considerable reduction of the turbulence level and the production of turbulent kinetic energy. In fact, by this strategy the shear flow transient growth mechanism is activated and the formed spanwise mean flow is an *intrinsic, nonlinear composition* of the controlled turbulence and not directly introduced in the system. In the present paper, a weak near-wall volume forcing is designed to impose the velocity perturbations with required characteristics in the flow. The efficiency of the proposed scheme has been demonstrated by direct numerical simulation using plane Couette flow as a representative example. A promising result was obtained: after a careful parameter selection, the forcing reduces the turbulence kinetic energy and its production by up to one-third. The strategy can be naturally applied to other wall-bounded flows, e.g. channel and boundary-layer flows. Of course, the considered volume force is theoretical and hypothetical. Nevertheless, it helps to gain knowledge concerning the design of the seed velocity field that is necessary to be imposed in the flow to achieve a significant reduction of the turbulent kinetic energy. This is convincing with regard to a new control strategy, which could be based on specially constructed blowing/suction or riblets, by employing the insight gained by the comprehension of the results obtained using the investigated methodology in this paper.

Key words: flow control, turbulence control, turbulent flows

† Email address for correspondence: george.khujadze@uni-siegen.de

1. Introduction

Investigations of problems concerned with a reduction of the energetic costs of moving (airplanes, ships, etc.) bodies in fluids, and also of fluids/fuels being transported in pipelines, have a century-long history. A wide variety of active and passive, linear and nonlinear flow control mechanisms for drag reduction have been suggested, tested, developed and implemented over the years. A comprehensive review and analysis of the problem can be found in the following publications (Choi, Moin & Kim 1993; Gad-el-Hak 2000; Bewley 2001; Kim 2003; Dean & Bhushan 2010). The comprehensive discussion of the subject is presented in the April 2011 issue of the *Philosophical Transactions of the Royal Society A*, on the theme: 'Flow-control approaches to drag reduction in aerodynamics: progress and prospects'.

It is now well recognized that coherent structures play an important role in wall-layer dynamics in wall-bounded turbulent flows (Robinson 1991). There is strong evidence (see e.g. Kim 2011; Garcia-Mayoral & Jimenez 2011 and references therein) that most high skin–friction regions in near-wall turbulent layers are induced by nearby streamwise vortices. The ubiquitous structural features in the near-wall region are streaks: spanwise modulation of the streamwise velocity. It has to be emphasized that the turbulent plane channel flow was one of the first cases where the large-scale streaks have been observed (Lee & Kim 1991). Common features of all drag-reduced flows are weakened near-wall streamwise vortices and streaks. In general, streamwise vortices are formed and maintained by a self-sustained dynamics of the turbulence. The latter is supported by the linear/unstable and nonlinear processes associated also with wall-layer streaks and streamwise-dependent disturbances.

Recently, efforts have been made to control turbulence through different spanwise wall-based forcing methods (see Karniadakis & Choi (2003) and references therein). These attempts address the modification of near-wall turbulence by direct creation of a spanwise flow. There are different ways of transverse flow generation, e.g. by using the simplified experimental and numerical models of shark-skin riblets (Goldstein, Handler & Sirovich 1995; Garcia-Mayoral & Jimenez 2011; Strand & Goldstein 2011), wall oscillations (Ricco *et al.* 2012; Touber & Leschziner 2012) and streamwise travelling waves (Quadrio, Ricco & Viotti 2009). However, there could be another, indirect way of a spanwise mean flow generation, for instance, by a week near-wall forcing that activates the shear flow transient growth mechanism and, finally, results in the breaking of turbulence spanwise reflection symmetry which in turn, leads to the turbulence control. The scheme of this control strategy is the following:

(i) a specially designed (non-symmetric in spanwise direction) near-wall weak forcing generates, so-called, optimal seed velocity perturbations that extract shear flow energy and undergo substantial transient growth (it is worth noting here that the perturbations that undergo a maximum energy growth in the characteristic dynamical time of the flow are called the optimal perturbations; see e.g. Farrell & Ioannou (1993) and Farrell & Ioannou (2000));

(ii) the amplified non-symmetric velocity perturbations lead to the breaking of the turbulence spanwise reflection symmetry and the generation of mean spanwise flow;

(iii) the latter, in turn, changes the balances/statistics of the turbulence and results in a significant reduction of its level.

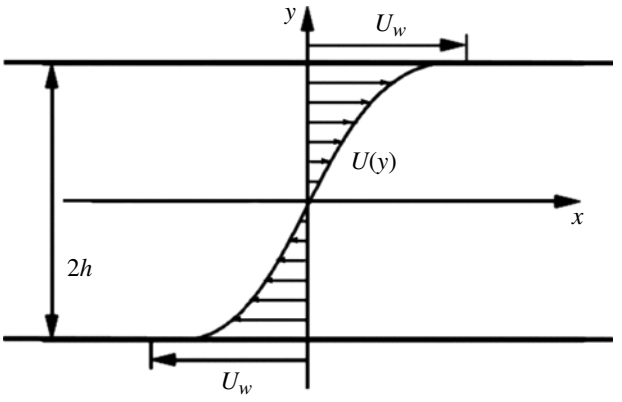

FIGURE 1. The flow geometry in plane Couette flow.

Thus, the suggested control strategy proposes a permanent (at each simulation time step) imposition of helical seed optimal velocity perturbations with special length scales in the flow that have the potential for quite fast transient growth. Subsequently, these perturbations effectively induce the helical nature to the turbulence. In this work the proposed strategy was realized in the example of a weak, helical near-wall forcing (active control) of plane Couette flow. However, it is obvious that the imposition of seed perturbations in order to initiate the above-introduced strategy can also be achieved by a well-designed blowing/suction active control or by passively introducing wall roughness. This strategy can be naturally extended to any wall-bounded flows.

The outline of the paper is as follows: § 2 provides the details about the numerical requirements of the numerical simulations performed; § 3 gives the description of the weak, helical near-wall forcing; the direct numerical simulations (DNS) and analysis of the results of the flow control are presented in § 4; and, finally, the conclusions are given in § 5. Furthermore, the validation of numerical simulations of plane Couette flow is presented in the appendix A.

2. Numerical requirements

The incompressible canonical plane Couette flow with the Reynolds number $Re \equiv U_w h/\nu$, based on the wall velocity U_w, the channel half-width h, and the kinematic viscosity ν is considered (see the figure 1). The shear parameter of the flow is defined as the ratio of the wall velocity to the channel half-width, $A \equiv U_w/h$. The plane Couette flow has a monotonic turbulent velocity profile. We denote by (x, y, z) the streamwise, wall-normal and spanwise directions respectively. No-slip boundary conditions are used on the walls. A pseudo-spectral code which was developed at the Royal Institute of Technology (KTH), Stockholm was used in our simulations (details of the code can be found in Skote (2001) and Lundbladh, Henningson & Johansson (2004)). Fourier decomposition in horizontal (x and z) and Chebyshev discretization in wall-normal (y) directions were applied. Hence, the spectral methods were used in all spatial directions, which gives a highly accurate discretization of the governing equations. For further details about the spectral discretizations and additional references see Canuto *et al.* (2006). Time integration was performed using a third-order Runge–Kutta method for the advective and forcing terms and Crank–Nicolson for the viscous terms. The time step was determined by

the CFL number and was adjusting itself automatically to the actual flow situation. All quantities were normalized by U_w and h. The original code was modified to implement the forcing presented by (3.1)–(3.8).

Simulations at different parameters of the controlled and uncontrolled Navier–Stokes equations have been performed at $Re = 750$. The corresponding turbulent Reynolds number based on friction velocity ($u_\tau = \sqrt{\tau_w/\rho}$) and channel half-width was $Re_\tau = hu_\tau/\nu = 52$ which is a factor two higher than the lowest Reynolds number for which turbulence is sustained (Komminaho, Lundbladh & Johansson 1996). The simulations with two different sizes of computational domains were carried out at different numbers of grid points. For details of the code validation, numerical parameters and the convergence tests see the appendix A. The computation domain size ($L_x \times L_y \times L_z$), number of grid points ($N_x \times N_y \times N_z$), spatial ($\Delta x^+ \times \Delta y^+ \times \Delta z^+$) and time resolutions ($\Delta t u_\tau/\nu = \Delta t^+$), sampling time ($tU_w/h$ and tU_w/L_x) are given in table 2. The superscript '+' means the normalization of the quantities with the kinematic viscosity ν and with the friction velocity u_τ. Here we would like to emphasize that the analysis of our numerical simulations has shown that an increase in number of modes and size of the simulation domain did not change the results. As for the time scales, the simulations were performed for long time intervals to obtain well-converged flow statistics. The numerical experiments were run for a total of $tU_w/h = 10\,000$ time units. The first $tU_w/h = 3000$ (corresponding to $tU_w/L_x = 118$) time units were used to obtain a fully developed turbulent flow. Then, the forcing was switched on, and the simulations were run more than $tU_w/h = 7000$ ($tU_w/L_x = 277$) time units. In wall units, the non-dimensional time step was $\Delta t^+ = 0.1$ which is even smaller than that presented in Tsukahara, Kawamura & Shingai (2006). The integration time is sufficient to get smooth statistics and good integral quantities. Thus, our numerical simulations are in full agreement with the results published in the literature on the subject.

3. Model of non-symmetric near-wall weak forcing

The transient growth of perturbations (that is due to the non-normality of the linearized dynamical operators of the shear flow system) is the basis of the dynamical activity of smooth shear flows. It is well known that smooth shear flows support a set of perturbations (called optimal) that undergo large transient growth during the dynamical time of the turbulence for sufficiently high Reynolds numbers. This time can be defined by the characteristic time of nonlinear processes and should be $\mathcal{O}(1/A)$. In general, in smooth shear flows a robust growth appears for three-dimensional perturbations satisfying the following conditions (see Craik & Criminale 1986; Farrell & Ioannou 1993):

(i) the length scales in streamwise and spanwise directions are of the same order but larger than the viscous dissipative length scale, $\ell_x \simeq \ell_z \gg \ell_\nu$ or, in terms of wavenumbers, $k_x, k_z \ll k_\nu$ (here, $k_\nu \equiv \sqrt{Re} \approx 1/\ell_\nu$);

(ii) the perturbations are tilted with the background shear or, in terms of wavenumbers, $k_y/k_x < 0$. These general conditions encouraged us to implement the following helical near-wall forcing for the considered flow (see figure 2):

$$F_x(x, y, z) = A_1 f(y) \cdot \sum_{n,m=0}^{N,M} Z_m \cdot \exp(-X_n^2 - Z_m^2) \exp\left(-\frac{\hat{X}_n^2}{l_x^2} - \frac{\hat{Z}_m^2}{l_z^2}\right), \tag{3.1}$$

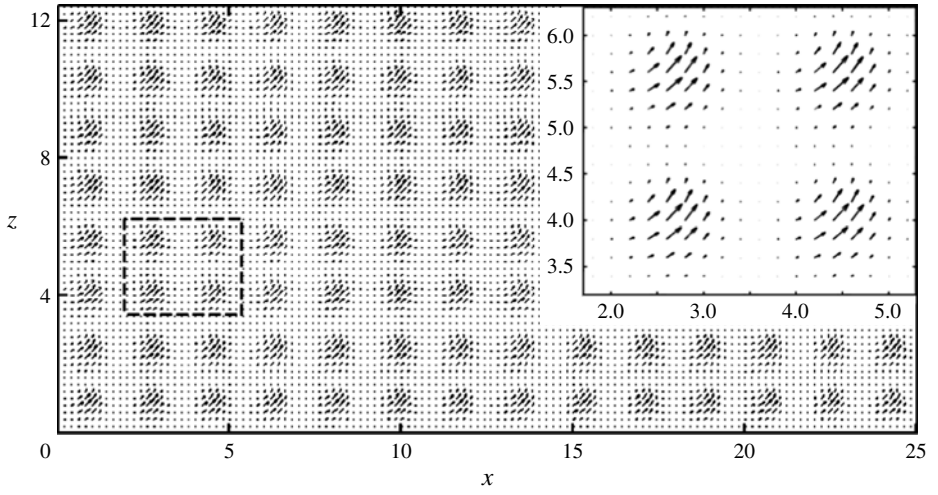

FIGURE 2. Design of the helical forcing in the xz plane at $y = -y_{peak} = -0.95$ and parameters $M = 7$, $N = 13$, $a = 1.2221$, $\phi = \pi/4$, $\ell_x = \ell_z = 1/\sqrt{10}$, $\ell_y = 0.2$, $A_1 = 0.4$ and $A_2 = 0.008$.

$$F_y(x, y, z) = -A_2 \cdot f(y) \cdot \sum_{n,m=0}^{N,M} \exp(-X_n^2 - Z_m^2) \exp\left(-\frac{\hat{X}_n^2}{l_x^2} - \frac{\hat{Z}_m^2}{l_z^2}\right), \tag{3.2}$$

$$F_z(x, y, z) = -A_1 f(y) \cdot \sum_{n,m=0}^{N,M} X_n \cdot \exp(-X_n^2 - Z_m^2) \exp\left(-\frac{\hat{X}_n^2}{l_x^2} - \frac{\hat{Z}_m^2}{l_z^2}\right), \tag{3.3}$$

where

$$f(y) = \sin(\pi y) \exp\left[-\frac{(|y| - y_{peak})^2}{l_y^2}\right], \quad y \in [-1, 1] \tag{3.4}$$

with functions $X_n, Z_m, \hat{X}, \hat{Z}$ on the bottom wall ($y = -1$):

$$X_n(a, \phi) = \frac{x}{a} - 2n\cos\phi, \quad Z_m(a, \phi) = \frac{z}{a} - 1 - (4m + 1)(1 - \sin\phi), \tag{3.5}$$

$$\hat{X}_n(a, \phi) = \frac{x}{a} - (2n + 1)\cos\phi, \quad \hat{Z}_m(a, \phi) = \frac{z}{a} - (4m + 2)(1 - \sin\phi), \tag{3.6}$$

with functions $X_n, Z_m, \hat{X}, \hat{Z}$ on the top wall ($y = 1$):

$$X_n(a, \phi) = \frac{L_x - x}{a} - 2n\cos\phi, \quad Z_m(a, \phi) = \frac{L_z - z}{a} - 1 - (4m + 1)(1 - \sin\phi), \tag{3.7}$$

$$\hat{X}_n(a, \phi) = \frac{L_x - x}{a} - (2n + 1)\cos\phi, \quad \hat{Z}_m(a, \phi) = \frac{L_z - z}{a} - (4m + 2)(1 - \sin\phi), \tag{3.8}$$

where $L_x = 2a(N - 1)\cos\phi$ and $L_z = 4aM(1 - \sin\phi)$ are sizes of the simulation box and $N + 1$ and $M + 1$ are numbers of the forcing centres in the streamwise and spanwise directions, respectively; a and ϕ define the configuration of the forcing (a

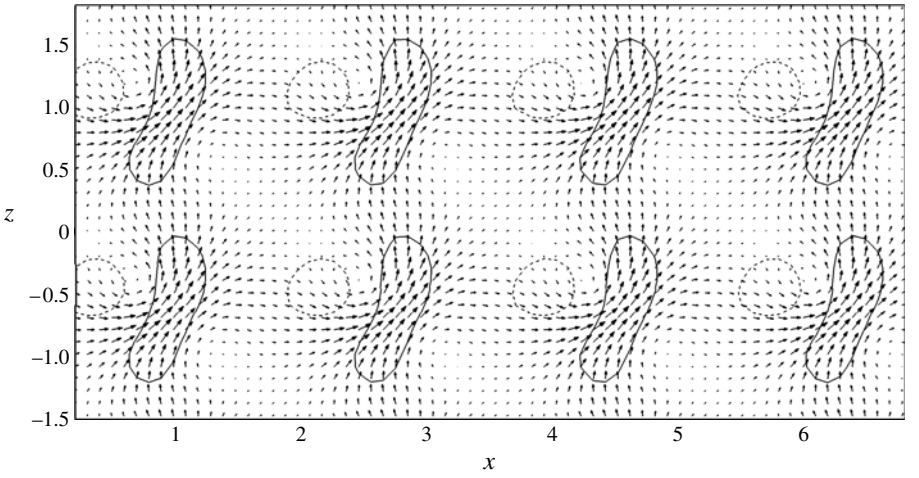

FIGURE 3. Seed velocity field in the xz plane ($y = -y_{peak} = -0.95$): the vector field with the contours of positive 0.0005 (—) and negative −0.0001 (– – –) spanwise velocity.

defines the size of the forcing 'cells' and ϕ is the forcing orientation in the xz plane, e.g. at $\phi = \pi/4$ quasi-equipartition of the forcing in the streamwise and spanwise directions occurs); l_x, l_y and l_z are the length scales related to the forcing localization in the streamwise, wall-normal and spanwise directions; A_1 and A_2 define the forcing amplitudes in the streamwise/spanwise and wall-normal directions; $X_n(a, \phi)$ and $Z_m(a, \phi)$ define the location of the forcing symmetry centres and $\hat{X}_n(a, \phi)$ and $\hat{Z}_m(a, \phi)$ define the location of the forcing localization centres in the streamwise and spanwise directions, respectively; and, finally, y_{peak} is the location of the forcing localization centre in the wall-normal direction.

4. Results of numerical study of the flow control

The numerical simulations of the plane Couette flow at a Reynolds number of $Re = 750$ and different sets of parameters for the non-symmetric near-wall volume forcing (see (3.1)–(3.8)) were performed. The statistics and instantaneous velocity fields of the uncontrolled and controlled turbulence were compared. The forcing (figure 2) causes the generation of a specially designed seed velocity perturbations at each simulation time step.

Figure 3 shows an xz slice of such a seed velocity field at $y = -0.95$ and for contour values of 0.0005 (solid line) and −0.0001 (dashed line) of the spanwise velocity component. It is obvious that the velocity field presented in figure 3 does not exactly mimic the forcing design: the continuity equation limits the possible flow movement. The vector field in the area of the solid contour initiates the breaking of the spanwise symmetry. The velocity field in the area of the dashed contour is due to the incompressibility condition (the continuity equation) and is unfavourable to the spanwise symmetry breaking. Nevertheless, the imposed velocity configuration, for the set of parameters presented in figure 2 (see the caption for the values of the parameters), initiates a robust transient growth and the generation of mean spanwise velocity. That, finally, leads to substantial reduction of the turbulent kinetic energy.

It is well known that Couette flow is spectrally stable, turbulence exhibits a subcritical nature manifesting itself in the bypass transition to turbulence. The

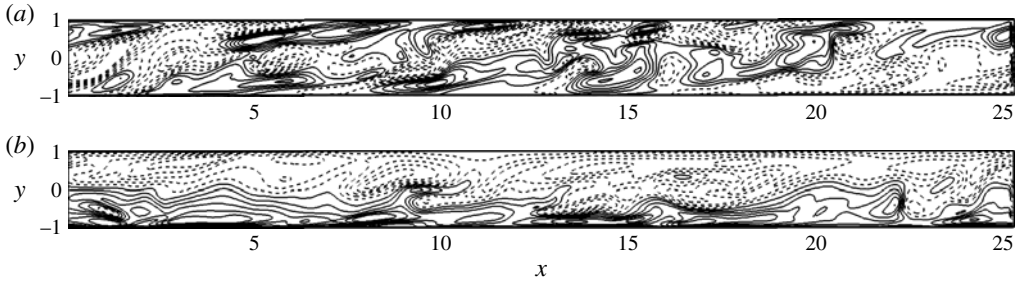

FIGURE 4. Contours of spanwise velocity in xy-plane for uncontrolled (a) and controlled (b) flows. Contours for $u_z > 0$ (—) and $u_z < 0$ (– – –) in the range of $[-0.2, 0.2]$ with increment 0.02 are presented.

proposed strategy/route of the flow control is based on peculiarities of linear and nonlinear processes in the framework of the bypass concept. According to this concept, the self-sustenance of the turbulence is the result of the linear transient growth of the perturbations' kinetic energy and positive nonlinear feedback induced by the flow non-normality, the role of nonlinearity in this case is principally different from its role in the Kolmogorov theory. The level/balance of turbulence depends on the nonlinear redistribution process in wavenumber space. One can impact this process indirectly, causing a change in the spectrum via the near-wall forcing. As a result the balance between linear and nonlinear processes can be achieved at different levels (low or high) of the turbulence. So, the imposed and specially designed initial seed perturbations undergo transient growth and become quite powerful. Consequently, these perturbations become an active participant of the nonlinear redistribution process, change it and lead to the balance at a low level of turbulence. It was found that the production of turbulent kinetic energy and turbulence level at the balance is very sensitive to the forcing parameters. By the DNS it was shown that the proposed strategy of the flow control is promising. In this paper, the attention is mainly given to the results of the numerical simulations that lead to the significant reduction of the turbulent kinetic energy production.

4.1. *Qualitative analysis of the uncontrolled and controlled flows: instantaneous velocity and vorticity fields*

Contours of the spanwise velocity component for the uncontrolled (a) and controlled (b) turbulence in xy plane are shown in figure 4. The levels of contours are in the range of $[-0.2, 0.2]$ with increment 0.02. Dashed and solid contours correspond to the negative and positive spanwise velocities correspondingly. In the case of uncontrolled turbulence, the contours with different signs are uniformly distributed in wall-normal direction. As was expected, no preferred direction is observed for the spanwise velocity: no mean flow in this case. A completely different picture is observed in figure 4(b). At first, the contours become rare, that indicates a reduction of the turbulence intensity. Second, the contours with negative values are mainly located in the upper half of the flow and the contours with the positive values in the lower half. This means the appearance of the mean flow in the spanwise direction.

Figure 5 displays the isosurfaces of instantaneous fields of the spanwise component of velocity for uncontrolled (a) and controlled (b) turbulent flows. The figure confirms the creation of mean spanwise velocity in the latter case showing that the isosurfaces

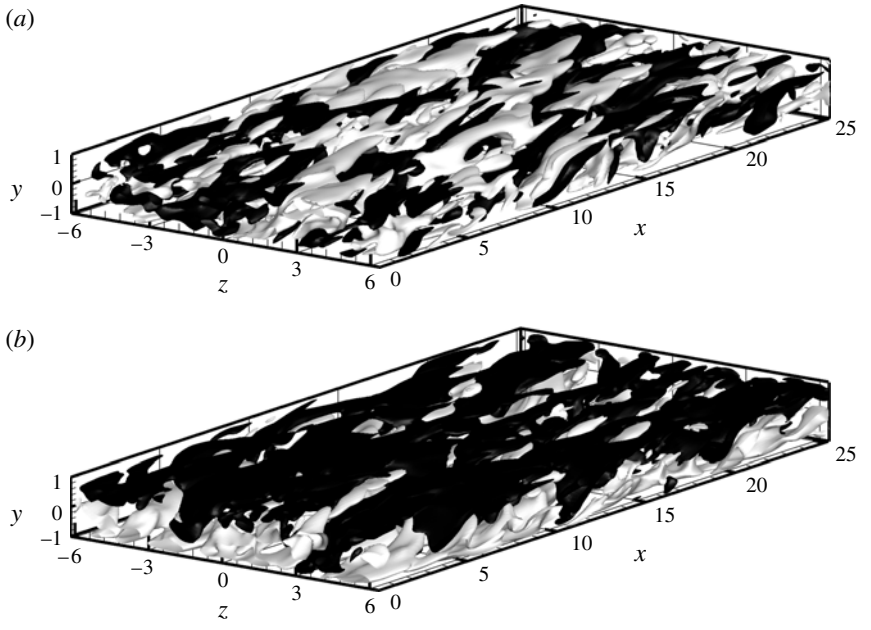

FIGURE 5. Isosurfaces ($u_z = -0.13$ black and $u_z = 0.13$ white) of spanwise velocity fields for uncontrolled at $t < 3000$ (a) and controlled at $t > 3000$ (b) flows.

with positive and negative signs are populated in the lower and upper half of the numerical domain, respectively.

The instantaneous velocity (wall-normal and spanwise components) and vorticity (spanwise component) fields in the xz plane at $y = 0$ (middle of the channel) are presented in figures 6 and 7 (in the form of a greyscale coding) for uncontrolled and controlled flows. In figures 6(a) and 7(a) we see the typical quantitative picture of the fully developed turbulent Couette flow where the black (minimum amplitudes) and white (maximum amplitudes) colour distribution is pronounced. As for the controlled flow the situation is noticeably different. The dominance of grey colour (intermediate amplitudes) is clearly observed in the plots (figures 6b and 7b) and the velocity and vorticity fields are significantly smoother, i.e. the level of small-scale perturbations in the controlled case is remarkably decreased. The reduction of the turbulent small scales (less dissipation on small scales), actually, indicates an absence of Kolmogorov's concept/scheme in the flow: the dynamics of self-sustenance of turbulence in the flow is now caused by the linear transient growth of the kinetic energy of the perturbations and positive linear feedback induced by the non-normality of the flow. The quantitative information about the large scales can be obtained from the analysis of the two-point correlation functions that will be given in the next section.

4.2. *Quantitative analysis of the controlled flow turbulence: one- and two-point statistics*

The statistics of the Reynolds stress tensor components in uncontrolled (dashed lines) and controlled (solid lines) cases are shown in figure 8. These plots show that the level of turbulence decreases significantly in the latter case. In addition to $\overline{u'_x u'_y}$ the

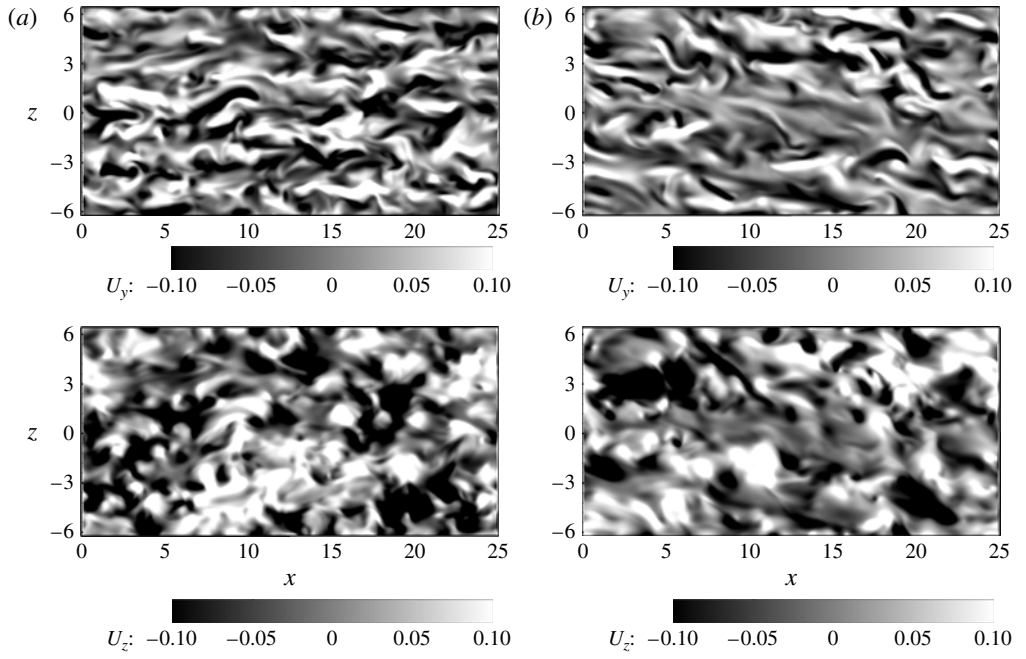

FIGURE 6. Instantaneous velocity (u_y, u_z) fields in the xz plane at $y = 0$ (a) for uncontrolled ($t = 3000$) and (b) controlled turbulent flows ($t = 10\,000$).

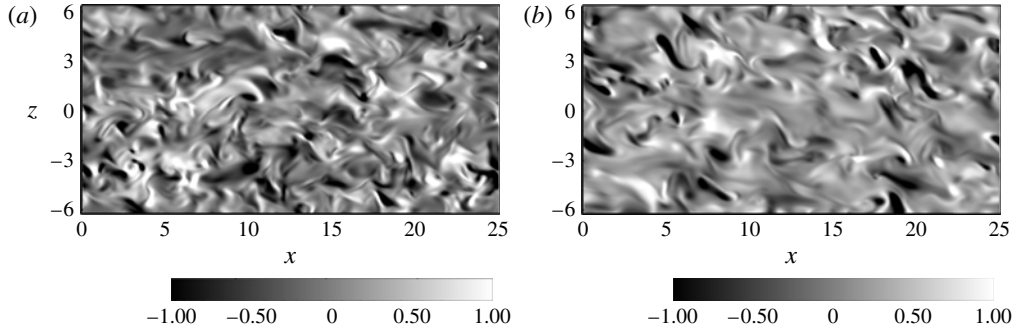

FIGURE 7. Instantaneous vorticity fields (ω_z) in the xz plane at $y = 0$ (a) for uncontrolled ($t = 3000$) and (b) controlled turbulent flows ($t = 10\,000$).

new non-diagonal Reynolds stress components ($\overline{u'_x u'_z}$ and $\overline{u'_y u'_z}$) appear. Thus in the case of the controlled flow all terms of Reynolds stress tensor are non-zero.

The maximum values of turbulence quantities in uncontrolled and controlled cases are given in table 1. Figure 9 shows the deviation of the controlled flow mean streamwise ($\Delta\overline{U}_x = \overline{U}_x^{contr} - \overline{U}_x^{turb}$) and spanwise ($\Delta\overline{U}_z = \overline{U}_z^{contr} - \overline{U}_z^{turb}$) velocity profiles from the profiles of the uncontrolled turbulent flow. The forcing does not create mean wall-normal flow. Figure 9(a) shows that the maximum deviation of mean streamwise velocity is quite small in the controlled flow: $\Delta\overline{U}_{x,max} \approx 0.014$. For the uncontrolled turbulent flow, the mean spanwise velocity is zero, consequently, in

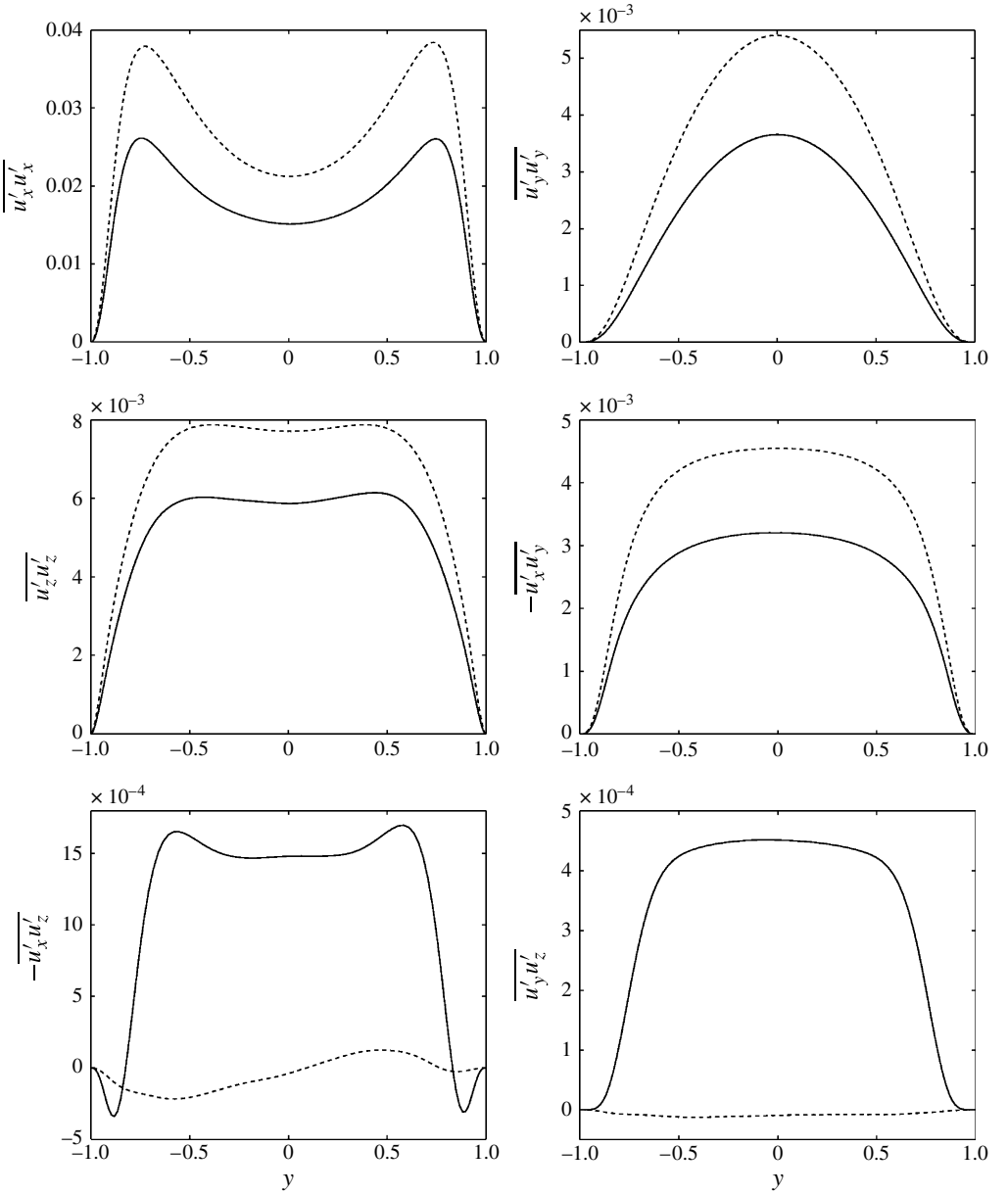

FIGURE 8. Comparison of Reynolds stress tensor components for uncontrolled (– – –) and controlled (—) turbulent flows.

the controlled case, $\Delta\overline{U}_z$ is defined by $\overline{U}_z^{contr}$, $\Delta\overline{U}_z = \overline{U}_z^{contr}$. One has to note that the mean spanwise velocity appears with the maximum value $\overline{U}_{z,max}^{contr} \approx 0.07$.

In figure 10 all components of the root-mean-square (r.m.s.) vorticity fluctuations for uncontrolled and controlled turbulent flows are presented. The limiting value of the relative streamwise turbulence intensity, $u_{x,rms}/U_w$, or equivalently $\omega^+_{z,rms} = \omega_{z,rms}\nu/u_\tau^2$ has been a subject of much debate in the literature. Based on measurements it has

Case	$u^+_{rms,max}$	$u^+_{rms,CL}$	$\omega^+_{z,max}$	Pr_x^{max}	Pr_z	P_x^{in}	$P^{in}_{z,max}$	Λ_{11x}
Uncontrolled	2.77	2.11	0.41	4.3	0	0	0	3.93
Controlled	2.36	1.76	0.28	0.29	0.5×10^{-4}	1×10^{-4}	4.8×10^{-4}	2.08

TABLE 1. Peak values of statistically averaged quantities at the simulation box $8\pi \times 2 \times 4\pi$ and number of modes $256 \times 97 \times 128$: turbulence intensity (u^+_{rms}), spanwise vorticity (ω^+_z), turbulence kinetic energy production (Pr_x and Pr_z), power input (P^{in}_x and P^{in}_z).

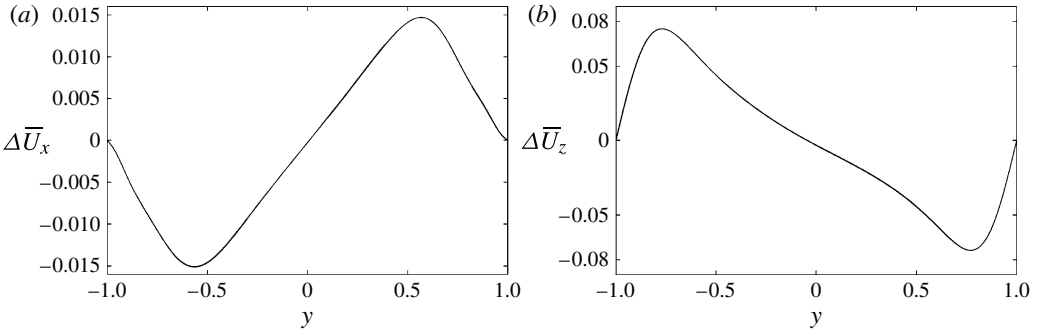

FIGURE 9. Deviation of the controlled flow mean (*a*) streamwise, $\Delta\overline{U}_x$, and (*b*) spanwise, $\Delta\overline{U}_z$, velocity profiles from the profiles of the uncontrolled turbulent flow the mean spanwise velocity of which is zero and $\Delta\overline{U}_z = \overline{U}_z^{contr}$.

been found that it should be in the range of 0.40–0.41 in the case of fully developed uncontrolled turbulent plane Couette flow (Komminaho *et al.* 1996). As one can see from the dashed line in figure 10(*c*) the maximum value of $\omega^+_{z,rms}$ approaches 0.41 which agrees well with the value accepted in the literature. In the case of controlled flow all components of the r.m.s. vorticity fluctuations (solid lines in figure 10) undergo significant decay: the maximum of $\omega^+_{z,rms}$ reduces to 0.24.

Two-point correlation functions, $R_{11}(r_1) = \overline{u_1'(x_1)u_1'(x_1+r_1)}/\overline{u_1'(x_1)u_1'(x_1)}$ (*a*) and $R_{11}(r_3) = \overline{u_1'(x_1)u_1'(x_1+r_3)}/\overline{u_1'(x_1)u_1'(x_1)}$ (*b*), for uncontrolled and controlled turbulent flows are presented in figure 11. (The definition of two-point correlation functions can be found in appendix A (see (A 2)). The integral length scales in the streamwise direction in the controlled case become smaller as can be observed from figure 11(*a*) (solid line). Concerning the spanwise two-point correlation function in case of controlled flow only one period of positive–negative regions is observed. This is expected because of the generation of the mean spanwise velocity. In figure 12 the streamwise integral length scale ($\Lambda_{11x} = \int_0^\infty R_{11}(r_1)\mathrm{d}r_1$) is presented for controlled flow. The solid line displays the time evolution of Λ_{11x} that converges to the mean value of $\Lambda_{11x} = 2.08$ (dashed line) that is half the value in the case of uncontrolled flow (see figure 23). As is shown in the appendix A the simulation box used in our study is adequate to resolve the uncontrolled flow. It can be seen in figure 12 that the streamwise integral length scale considerably decreases in the controlled flow. Thus, we can state that the dimension of the simulation box is large enough in the controlled case too.

Besides the classical term in turbulent kinetic energy production $\mathrm{Pr}_x = -\overline{u_x'u_y'}\mathrm{d}\overline{U}_x/\mathrm{d}y$, the additional spanwise component $\mathrm{Pr}_z = -\overline{u_y'u_z'}\mathrm{d}\overline{U}_z/\mathrm{d}y$, appears due to the forcing.

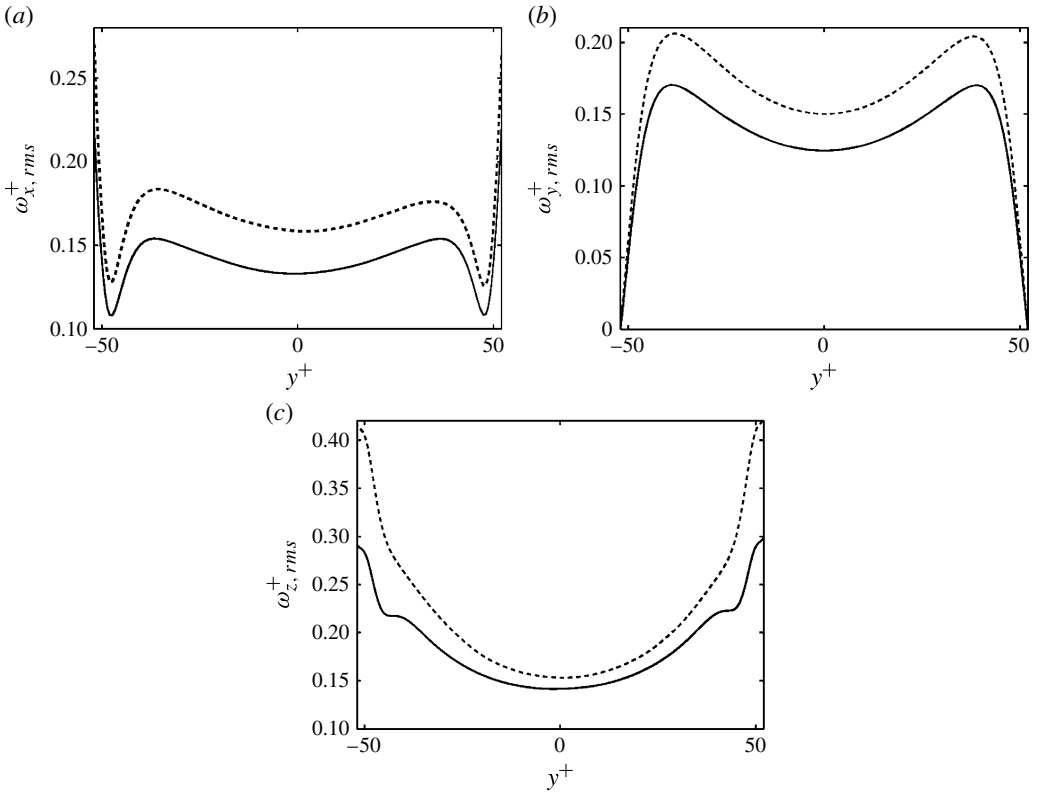

FIGURE 10. Root-mean-square of vorticity fluctuations for uncontrolled (– – –) and controlled (—) flows are presented in plus units ($\omega_{i,rms} \equiv \omega_{i,rms}\nu/u_\tau^2$).

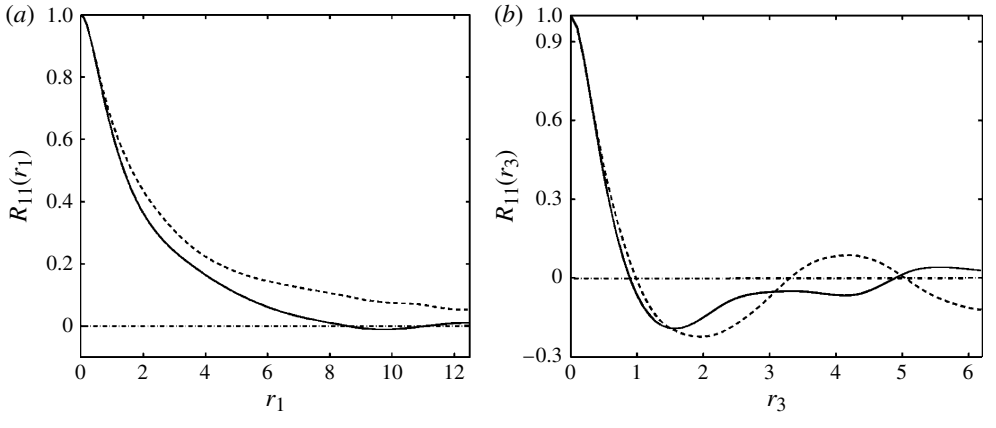

FIGURE 11. The two-point correlation functions for streamwise velocity R_{11} at $y = 0$ for (*a*) streamwise, r_1, and (*b*) spanwise, r_3, separations: uncontrolled (– – –) and controlled (—) turbulent flows.

Defining the input power in the flow, one has to take into account the following: the forcing is steady in time, but varies in physical space (see (3.1)–(3.3)). Therefore,

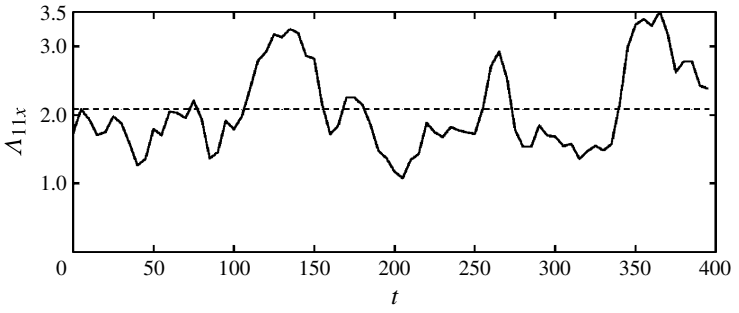

FIGURE 12. The streamwise integral length scale for the controlled flow: time evolution of Λ_{11x} (—); time-averaged value $\Lambda_{11x} = 2.08$ (– – –).

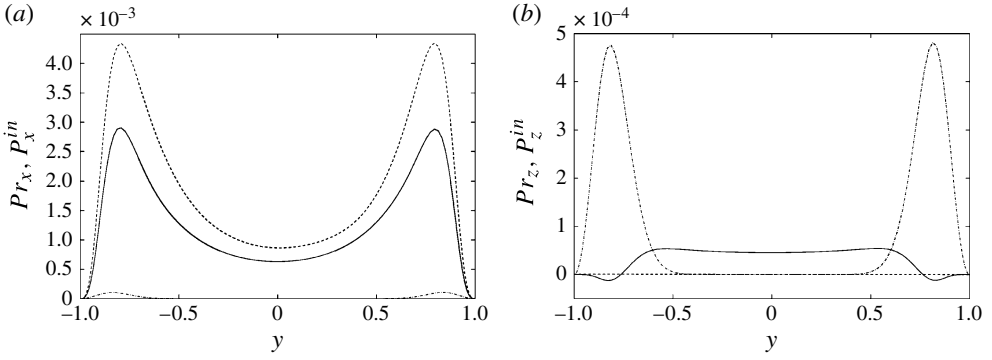

FIGURE 13. Time-averaged productions of turbulent kinetic energy. (*a*) The streamwise component of production, Pr_x for the uncontrolled (– – –) and controlled (—) turbulent flows and input power, P_x^{in} (– · –). (*b*) The same quantities for the spanwise components.

motionless fluid particles are influenced by the steady in time force, but moving fluid particles are influenced by varying forces. This means that the mean input power on the fluid particles moving with some constant velocity (e.g. mean velocity) is zero. Consequently, the input power in the flow should be defined by the varying (fluctuating) part of fluid particle velocity:

$$P^{in} = \overline{F_x u_x'} + \overline{F_y u_y'} + \overline{F_z u_z'} \equiv P_x^{in} + P_y^{in} + P_z^{in}. \tag{4.1}$$

It has to emphasized that P_y^{in} is negligible. The terms characterizing the energetics of the control process (as a function of wall-normal coordinate) are presented in figure 13. Figure 13(*a*) displays P_x^{in} (dashed-dotted line) and Pr_x for the uncontrolled (dashed line) and controlled (solid line) flows. Figure 13(*b*) displays the same for the spanwise components. The figure shows that $P_x^{in}, P_z^{in}, \mathrm{Pr}_z \ll \mathrm{Pr}_x$ and the turbulent kinetic energy production is substantially reduced in the controlled case (compare dashed and solid lines in figure 13(*a*)). This result is confirmed by figures 14 and 15 that display the time evolution of the production of turbulent kinetic energy averaged in the streamwise and spanwise directions and integrated in the wall-normal direction. The time region $t \leqslant 3000$ corresponds to the uncontrolled turbulent flow. The forcing

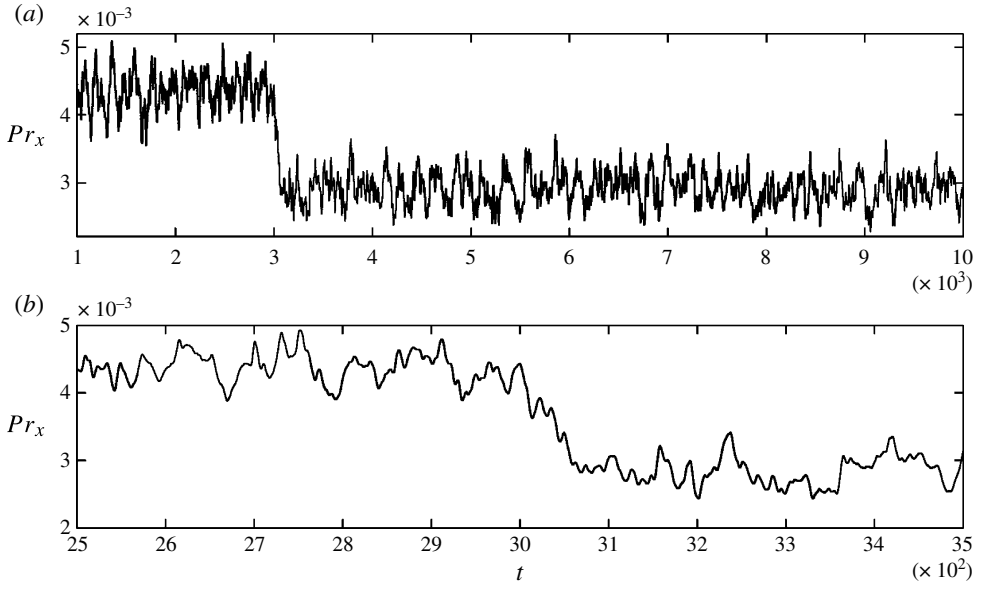

FIGURE 14. Time evolution of the production of turbulent kinetic energy (averaged in the streamwise and spanwise and integrated in the wall-normal directions) for the uncontrolled ($t < 3000$) and controlled ($t > 3000$) turbulent flows: (a) full simulation and (b) enlarged view of the time interval in the transition region.

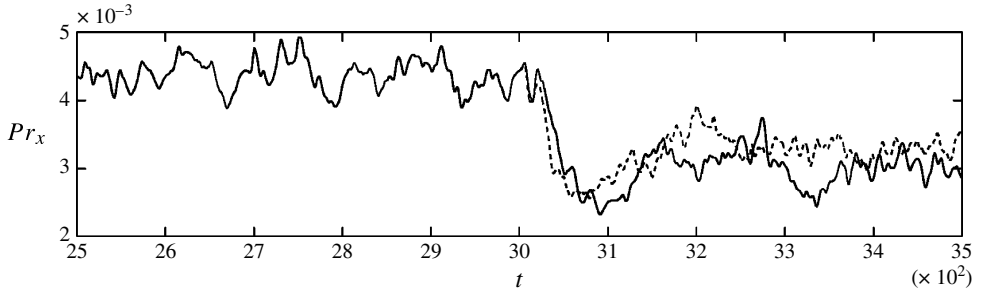

FIGURE 15. Time evolution of the production of turbulent kinetic energy (averaged in the streamwise and spanwise and integrated in the wall-normal directions) for the uncontrolled ($t < 3000$) and controlled ($t > 3000$) flows at two different locations of the forcing centres from the wall: $y_{peak} = 0.95$ (—) and $y_{peak} = 0.90$ (– – –).

was switched on at $t = 3000$. Hence, $t > 3000$ corresponds to the controlled flow. As a result, a reduction of the turbulent production by up to one-third was obtained (figure 14a). In figure 14(b) the zoomed time interval is shown in the transition region (from uncontrolled to the controlled case). As we see, the time interval during which the action of the forcing leads to the substantial reduction of turbulent kinetic energy production is very small (≈50 time units).

Figure 15 compares the time evolution of the production for two different locations of the forcing centre in the wall-normal direction. The figure shows that the shift

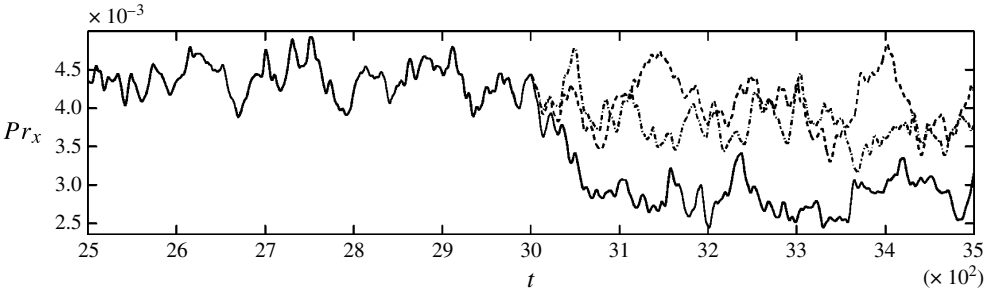

FIGURE 16. Time evolution of the production of turbulent kinetic energy for the uncontrolled ($t < 3000$) and controlled ($t > 3000$) flows at three different cases: with $\ell_y = 0.2$, $A_1 = 0.4$, $A_2 = 0.008$ (—); with $\ell_y = 0.1$, $A_1 = 0.4$, $A_2 = 0.008$ (– – –); with $\ell_y = 0.1$, $A_1 = 0.8$, $A_2 = 0.032$ (– · –).

of the forcing location from the wall (from $y_{peak} = 0.95$ to $y_{peak} = 0.90$) remarkably reduces the control of the flow. As is outlined in the comparison of figures 2 and 3, the continuity equation restricts the flow motion and the velocity field introduced by the forcing does not mimic the forcing design exactly: there appear the areas of the velocity field that are unfavourable to the spanwise symmetry breaking (the areas inside the dashed contours in figure 3). Apparently these areas are minimal at about $y_{peak} = 0.95$. Figure 16 shows that the decrease of the localization length scale (ℓ_y) along the wall-normal direction by a factor of two eliminates the efficiency of the control process (see the dashed line). Doubling the forcing amplitude achieves only a slight improvement in the control efficiency (see the dotted line). As we can see, obtaining the optimal geometry of the forcing requires delicate adjustment of the parameters that have to be fixed to obtain the substantial reduction of the turbulent kinetic energy production.

5. Conclusions

The aim of this study was to propose and analyse a new strategy/route of flow control imposing specially designed seed perturbations that have the potential for transient growth and lead to the generation of helical turbulence, which has non-zero streamwise vorticity with simultaneous creation of spanwise mean flow.

Taking into account the feature of the subcritical turbulence (see § 4) and definition of optimal perturbations (see the beginning of § 3) the model of near-wall body forcing with non-zero helicity was constructed and a DNS was performed to evaluate the efficiency of the proposed scheme on the example of plane Couette flow. The results are promising and encouraging: the applied forcing considerably reduces the kinetic energy production in comparison with the uncontrolled turbulent flow. Of course, the considered volume force is hypothetical. However, it helps to gain knowledge about the design of the seed velocity field, which, when permanently imposed in the flow (at each simulation time step) leads to a substantial reduction of the turbulent kinetic energy. The observed results support the vitality of the proposed control strategy and initiate further investigations. It is obvious that the imposition of the needed/helical seed velocity perturbations can also be achieved by manipulation of the boundaries via an implementation of properly designed blowing/suction or riblets. This is principally not a difficult, but quite laborious issue and requires a separate investigation.

$L_x \times L_y \times L_z$	$N_x \times N_y \times N_z$	$\Delta x^+ \times \Delta y^+ \times \Delta y^+$	Δt^+	tU_w/L_x	tU_w/h
$8\pi \times 2 \times 4\pi$	$256 \times 97 \times 128$	$3.4 \times 0.03 - 1.6 \times 3.4$	0.1	$118 + 277$	$3000 + 7000$
$8\pi \times 2 \times 4\pi$	$512 \times 257 \times 256$	$1.7 \times 0.004 - 0.6 \times 1.7$	0.06	$158 + 39.5$	$4000 + 1000$
$16\pi \times 2 \times 8\pi$	$512 \times 257 \times 256$	$3.4 \times 0.004 - 0.6 \times 3.4$	0.06	$59.4 + 19.8$	$3000 + 1000$

TABLE 2. Computational parameters of the main simulations.

Acknowledgements

The authors gratefully acknowledge the funding from Deutsche Forschungsgemeinschaft (DFG) under grant numbers OB 96/13-2, OB 96/30-1 and KH 257/3-1. GKh is indebted to Dr Tsukahara, from Tokyo University of Science, for valuable discussions and providing his data.

Appendix. Validation of the DNS of plane Couette flow

In the following we give a detailed description of the parameters of the performed simulations. The results of convergence tests are given and discussed. In table 2 the important parameters of the performed DNS are summarized.

The turbulent mean velocity profiles in outer (*a*) and plus units (*b*) are plotted in figure 17. (The superscript '+' means the normalization of quantities with the kinematic viscosity ν and with the friction velocity u_τ.) As we see from figure 17(*a*), the profile from the present DNS collapses to that obtained by Tsukahara *et al.* (2006). A logarithmic region can be observed figure 17(*b*) where the same profile is presented but in plus units (solid line) and compared with the classical log law (dashed line). The log region is a well-defined borderline between fully developed turbulent and transitional flows. Consequently, the plane Couette flow studied in the paper is fully developed turbulent flow. The comparison of the DNS result with the theoretical one (log law) gives a well-acknowledged value of the von Karman constant $\kappa = 0.41$ that agrees with those found by others in plane Couette flow simulations and experiments (see the papers by Tsukahara *et al.* (2006) and Komminaho *et al.* (1996) and references therein).

Figure 18 demonstrates the grid convergence showing the production of turbulent kinetic energy as a function of the wall-normal coordinate for two different resolutions (*a*) and simulation domains (*b*). These plots show good convergence of the simulations for both cases and, consequently, the lower resolution and smaller box are sufficient to obtain physically reliable results. It has to be emphasized that the resolution of our simulations is the same as published in the literature and must be enough to resolve all relevant scales of the flow (Komminaho *et al.* 1996; Tsukahara *et al.* 2006). Thus, we can state that the size of the box of $8\pi \times 2 \times 4\pi$ is totally adequate for obtaining accurate quantitative data for the flow. To be more precise, once the statistically steady state is reached, the right- and left-hand sides of following equation

$$\tau^+_{total} = 1 = -\overline{u'_x u'_y}^+ + \frac{\mathrm{d}\overline{U_x}^+}{\mathrm{d}y^+} \tag{A 1}$$

must be balanced (well-known characteristic of the turbulent plane Couette flow). Here τ_{total} is the total shear stress, the distribution of which is given in figure 19 together with Reynolds shear stress and streamwise mean velocity derivative. The dashed line in the figure shows the total shear stress: $\tau^+_{total} = 1$ as was expected from the theory.

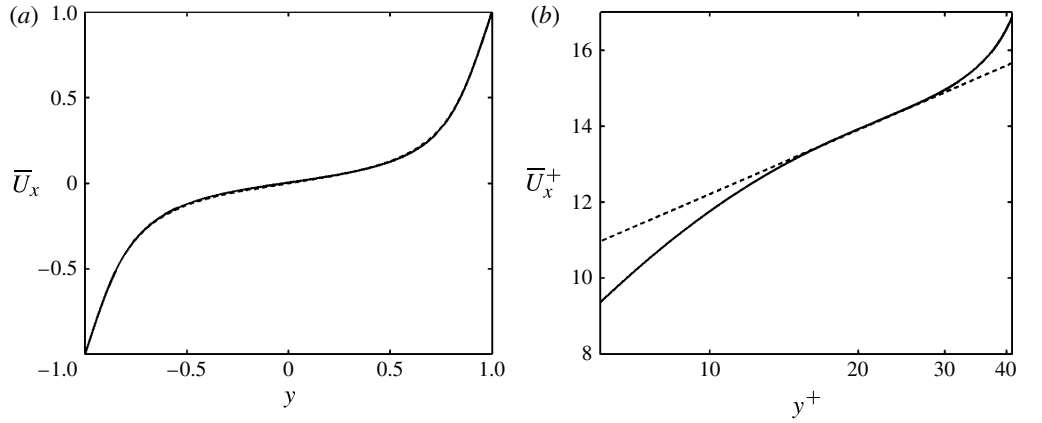

FIGURE 17. (*a*) Mean velocity profiles in outer units from the presented DNS of uncontrolled flow (—) compared with Tsukahara *et al.* (2006) data (– – –). (*b*) The same profile in plus units (—) and log-law $\overline{U}_x = 1/\kappa ln(y^+) + 5.1$ (– – –).

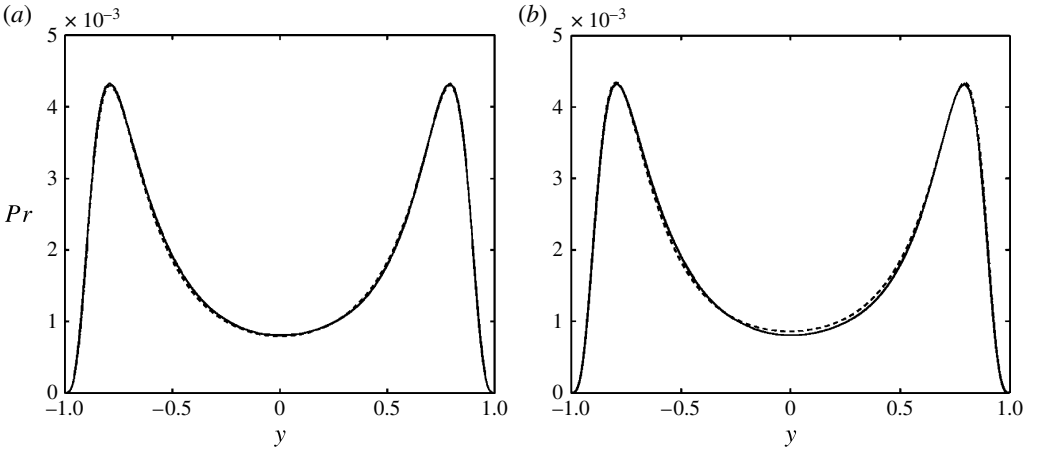

FIGURE 18. (*a*) Production of turbulent kinetic energy for $256 \times 97 \times 128$ (—) and $512 \times 257 \times 256$ (– – –) number of modes at the simulation box $8\pi \times 2 \times 4\pi$. (*b*) Comparison of production for different simulation domains $8\pi \times 2 \times 4\pi$ (– - –), $16\pi \times 2 \times 8\pi$ (—) at the number of modes $512 \times 257 \times 256$.

The effect of the simulation box size can be most clearly seen on the two-point correlation functions defined as follows:

$$R_{ij}(r_i) = \frac{\overline{u_i'(x_i)u_j'(x_i + r_i)}}{\overline{u_i'(x_i)u_j'(x_i)}}, \quad i, j = 1, 2, 3 \tag{A 2}$$

where r_1, r_2, r_3 are the separations between two different points in streamwise, wall-normal and spanwise directions correspondingly. In figure 20 we present two-point correlation functions for streamwise, wall-normal and spanwise components of velocity, R_{11}, R_{22}, R_{22} at $y = 0$ (centre of the channel) for the turbulent uncontrolled case calculated only for the half of the simulation box. In figure 20(*a*) one can

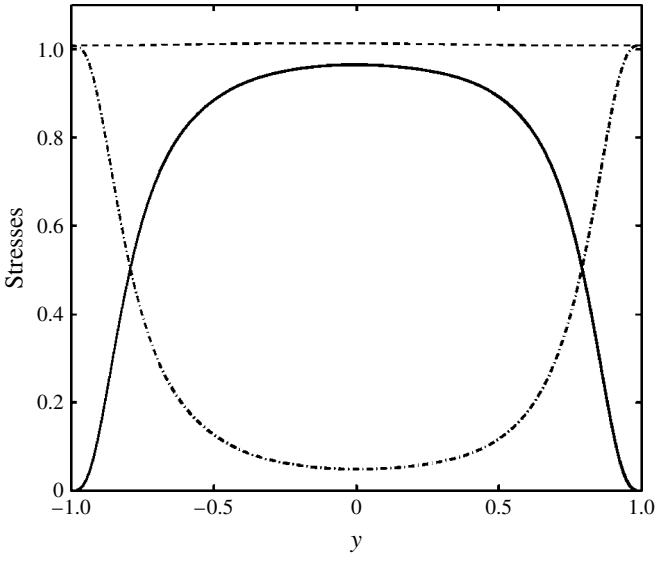

FIGURE 19. Reynolds ($\overline{u_x' u_y'}^+$) (– – –) and total shear (τ^+_{total}) (—) stresses. Wall-normal derivative of the streamwise mean velocity ($\mathrm{d}\overline{U_x}^+/\mathrm{dy}^+$) (– - –).

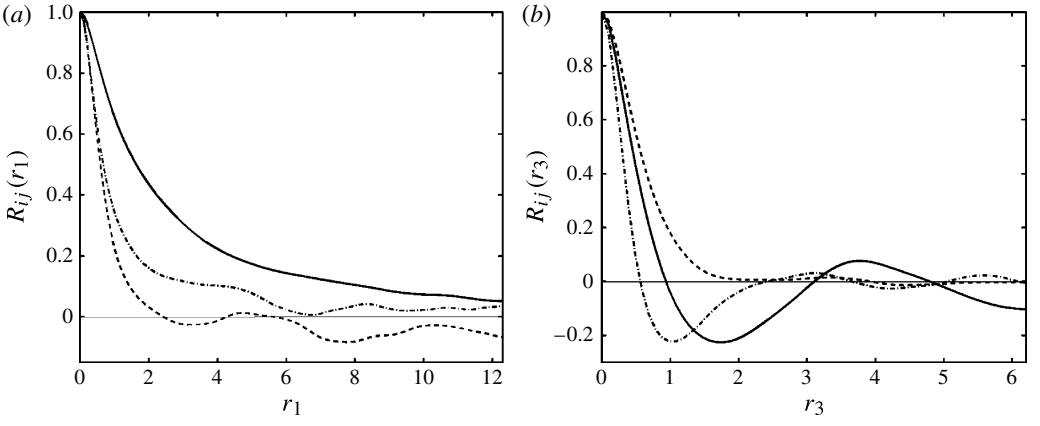

FIGURE 20. Two-point correlation functions for streamwise, R_{11} (—), wall-normal, R_{22} (– · –), and spanwise, R_{33} (– – –), velocities in the middle of channel versus r_1 (*a*) and r_3 (*b*) for simulation box $8\pi \times 2 \times 4\pi$.

observe that $R_{11}(r_1)$ decreases gradually to zero in the middle of the box, indicating that its length is enough to obtain the random meandering of the large structures within the computational domain. As for R_{22} and R_{33}, they decay even faster then R_{11}. Figure 20(*b*) displays the same two-point correlation functions but measured in the spanwise direction. As we see, the positive–negative regions of the correlation function appear which means that more than one long wavelength is captured in this direction. Figure 21 shows the two-point correlation function R_{11} versus r_1 (*a*) and r_3 (*b*) for different length of simulation boxes. The two-point correlation function for the small box (dashed line) follows those for the large box (solid line).

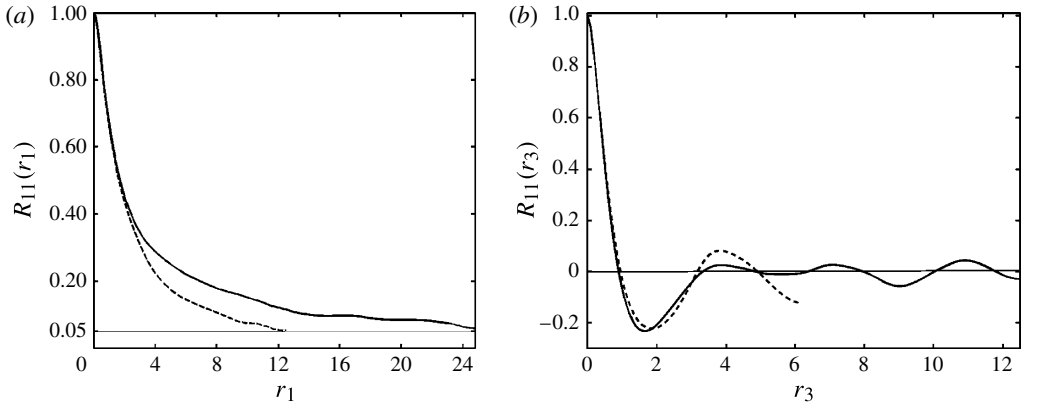

FIGURE 21. Two-point correlation functions for streamwise velocity R_{11} at $y = 0$ for (a) streamwise, r_1, and (b) spanwise, r_3, separations at different simulation domains: $16\pi \times 2 \times 8\pi$ (—); $8\pi \times 2 \times 4\pi$ (– – –).

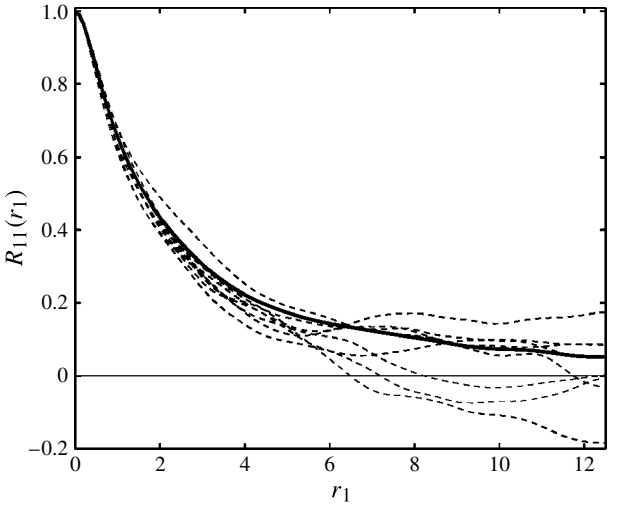

FIGURE 22. Streamwise two-point correlation functions, R_{11}, for different time realizations (– – –) and averaged over a long period of time (—).

We can see from figure 22 that $R_{11}(r_1)$ calculated at different time realizations fluctuate considerable. The solid line on this plot shows the average of $R_{11}(r_1)$ over a long period of time. Thus, in order to determine the $R_{11}(r_1)$ curve and integral length scales, we need to run the simulations for a very long time. Figure 23 represents the streamwise integral length scale (Λ_{11x}) that is defined as follows

$$\Lambda_{11x} = \int_0^\infty R_{11}(r_1)\mathrm{d}r_1. \tag{A 3}$$

The time evolution of $\Lambda_{11x}(t)$ (solid curve) converges to the value $\Lambda_{11x} = 3.93$.

To summarize, these numerical tests allow us to consider the resolution used in our study to be adequate, the box size used to be large enough and the integration time to be sufficient to give good statistics and integral quantities.

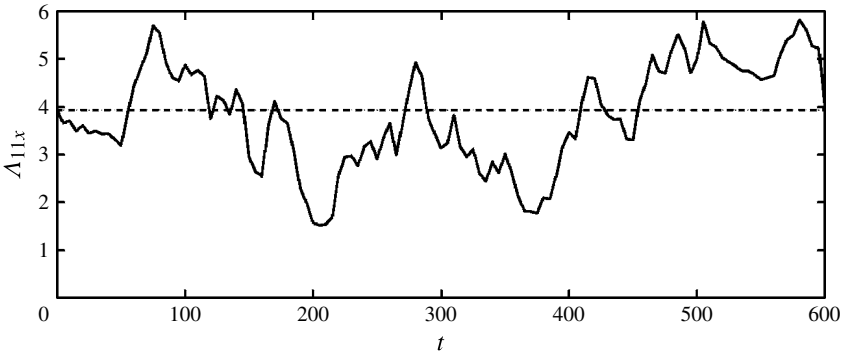

FIGURE 23. Streamwise integral length scale: time evolution of Λ_{11x} (—); time-averaged value $\Lambda_{11x} = 3.93$ (– – –).

REFERENCES

BEWLEY, T. R. 2001 Flow control: new challenges for a new renaissance. *Prog. Aerosp. Sci.* **37**, 21–53.

CANUTO, C., HUSSAINI, M. Y., QUARTERONI, A. & ZANG, TH. A. 2006 In *Spectral Methods* Fundamentals in Single Domains, Springer.

CHOI, H., MOIN, P. & KIM, J. 1993 Direct numerical simulation of turbulent flow over riblets. *J. Fluid Mech.* **255**, 503–539.

CRAIK, A. D. D. & CRIMINALE, W. O. 1986 Evolution of wavelike disturbances in shear flows: a class of exact solutions of the Navier–Stokes equations. *Proc. R. Soc. Lond.* A **406**, 13–26.

DEAN, B. & BHUSHAN, B. 2010 Shark-skin surfaces for fluid-drag reduction in turbulent flow: a review. *Phil. Trans. R. Soc.* A **368**, 4775–4806.

FARRELL, B. F. & IOANNOU, P. J. 1993 Optimal excitation of three-dimensional perturbations in viscous constant shear flow. *Phys. Fluids* A **5**, 1390–1400.

FARRELL, B. F. & IOANNOU, P. J. 2000 Transient and asymptotic growth of two-dimensional perturbations in viscous compressible shear flow. *Phys. Fluids* **12** (11), 3021–3028.

GAD-EL-HAK, M. 2000 *Passive, Active and Reactive Flow*. Cambridge University. Press.

GARCIA-MAYORAL, R. & JIMENEZ, J. 2011 Hydrodynamic stability and breakdown of the viscous regime over riblets. *J. Fluid Mech.* **678**, 317–347.

GOLDSTEIN, D., HANDLER, R. & SIROVICH, L. 1995 Direct numerical simulation of turbulent flow over a modelled riblet covered surface. *J. Fluid Mech.* **302**, 333–376.

KARNIADAKIS, G. E. & CHOI, K. -S. 2003 Mechanisms on transverse motions in turbulent wall flows. *Annu. Rev. Fluid Mech.* **35**, 45–62.

KIM, J. 2003 Control of turbulent boundary layers. *Phys. Fluids* **15**, 1093–1105.

KIM, J. 2011 Physics and control of wall turbulence for drag reduction. *Phil. Trans. R. Soc.* A **369**, 1396–1411.

KOMMINAHO, J., LUNDBLADH, A. & JOHANSSON, A. V. 1996 Very large structures in plane turbulent couette flow. *J. Fluid Mech.* **320**, 259–285.

LEE, M. J. & KIM, J. 1991 The structure of turbulence in a simulated plane couette flow. In *Eight Symp. on Turbulent Shear Flow* pp. 5.3.1–5.3.6. Technical University of Munich.

LUNDBLADH, A., HENNINGSON, D. & JOHANSSON, A. V. 2004 An efficient spectral integration method for the solution of the navier-stokes equations. *Tech. Rep.*, Department of Mechanics, KTH, S-100 44, Stockholm, Sweden.

QUADRIO, M., RICCO, P. & VIOTTI, C. 2009 Streamwise-travelling waves of spanwise wall velocity for turbulent drag reduction. *J. Fluid Mech.* **627**, 161–178.

RICCO, P., OTTONELI, C., HASEGAWA, Y. & QUADRIO, M. 2012 Changes in turbulent dissipation in a channel flow with oscillating walls. *J. Fluid Mech.* **700**, 77–104.

ROBINSON, S. K. 1991 Coherent motions in the turbulent boundary layer. *Annu. Rev. Fluid Mech.* **23**, 601–639.

SKOTE, M. 2001 Studies of turbulent boundary layer flow through direct numerical simulation. PhD thesis, Royal Institute of Technology, Department of Mechanics, Stockholm, Sweden.

STRAND, J. S. & GOLDSTEIN, D. B. 2011 Direct numerical simulations of riblets to constrain the growth of turbulent spots. *J. Fluid Mech.* **668**, 267–292.

TOUBER, E. & LESCHZINER, M. A. 2012 Near-wall streak modification by spanwise osscilatory wall motion and drag-reduction mechanisms. *J. Fluid Mech.* **693**, 150–200.

TSUKAHARA, T., KAWAMURA, H. & SHINGAI, K. 2006 DNS of turbulent Couette flow with emphasis on the large-scale structure in the core region. *J. Turbul.* **7** (19), 1–16.